Low-order models of wave interactions in the transition to baroclinic chaos

W.-G. Früh

Nonlinear Processes in Geophysics (1996) 3: 150–165

Nonlinear Processes in Geophysics

Low-order models of wave interactions in the transition to baroclinic chaos

W.-G. Früh

Sub-Department of Atmospheric, Oceanic, and Planetary Physics,
Department of Physics, Clarendon Laboratory,
University of Oxford, Oxford, OX1 3PU, UK

Received 8 February 1996 - Accepted 28 June 1996 - Communicated by K. Fraedrich

Abstract. A hierarchy of low-order models, based on the quasi-geostrophic two-layer model, is used to investigate complex multi-mode flows. The different models were used to study distinct types of nonlinear interactions, namely wave-wave interactions through resonant triads, and zonal flow-wave interactions. The coupling strength of individual triads is estimated using a phase locking probability density function.

The flow of primary interest is a strongly modulated amplitude vacillation, whose modulation is coupled to intermittent bursts of weaker wave modes. This flow was found to emerge in a discontinuous bifurcation directly from a steady wave solution. Two mechanism were found to result in this flow, one involving resonant triads, and the other involving zonal flow-wave interactions together with a strong β-effect.

The results will be compared with recent laboratory experiments of multi-mode baroclinic waves in a rotating annulus of fluid subjected to a horizontal temperature gradient.

1 Introduction

Since the earliest studies of Rossby waves in baroclinic fluids the two-layer model has played an important role. Phillips (1954) proposed the two-layer formulation as a discretised version of a continuously stratified baroclinic fluid, with a possible application as an idealised model of the general circulation of the atmosphere. Since then it has been used extensively in investigations of baroclinic instability (e.g. Pedlosky, 1987), weakly nonlinear behaviour of baroclinic waves (ibid. §7.16), or the dynamics of finite amplitude waves (e.g. Klein, 1990, for a review). It is generally agreed that the release of potential energy through baroclinic instability of the atmospheric circulation in middle latitudes is one of the most important factors in the development of planetary and synoptic weather patterns, which are the main agents for the poleward transport of heat and momentum. Once grown to finite amplitude, nonlinear dynamics dominate the evolution of these weather systems and give rise to complex—possibly chaotic—behaviour, thereby limiting the predictability of the weather, and even of the climate. Because it is highly idealised, the two-layer model provides a way to investigate fundamental aspects of the dynamics of baroclinic waves without the complications of more comprehensive and realistic models.

While far removed from realistic atmospheric situations, such models are much closer to laboratory experiments of baroclinic fluids. Laboratory counterparts to the model can be found in the mechanically forced two-layer experiment of e.g. Hart (1972) or Ohlsen and Hart (1989a), or in the thermally driven thermal annulus of e.g. Hide and Mason (1975). In the latter, the two-layer model is a vertical discretisation of a continuously stratified fluid. Both experimental systems were observed to exhibit a range of low-dimensional behaviour (e.g. Ohlsen and Hart, 1989a; Read et al., 1992). A low-order model with the essential ingredients should be able to produce qualitatively similar dynamics and bifurcation sequences.

Before the description of the model in §2, a brief summary of the main aspects of wave interactions are given in §1.1, followed by a description of the laboratory experiments which motivated this study. In §3, the model description is followed by an analysis of the linear stability of the imposed basic shear flow. The results from the integrations of the different model configurations are presented in §4 to §6, followed by a discussion in §7 and a short summary in §8.

1.1 Wave interactions

In rotating annulus experiments, Hide et al. (1977) observed strong phase locking of weaker modes to the dominant zonal wave mode of azimuthal wavenumber m.

Correspondence to: W.-G. Früh,

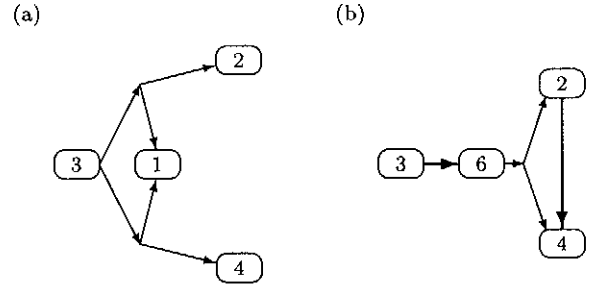

Fig. 1. Wave interaction mechanisms for the sideband coupling, (a) via the long wave, and (b) via the harmonic mode.

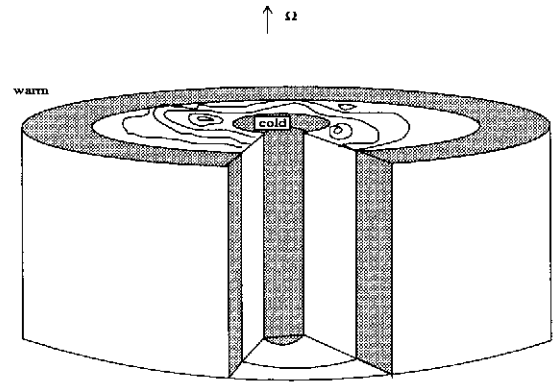

Fig. 2. Schematic diagram of the rotating annulus.

They proposed a mechanism of two resonant triads which, beside the dominant mode, involved the long wave with zonal wavenumber $m' = 1$, and either sideband, $m'' = m \pm 1$ (shown in Fig. 1 a). A different scenario was proposed by James et al. (1981) which did not involve the long wave. Instead, the coupling of the sidebands to the dominant mode was provided by the first harmonic of the dominant mode, $m' = 2m$, which could form a resonant triad with both sidebands, as illustrated in Fig. 1 (b) with $m = 3$ as the dominant mode. Both scenarios contain wave triads which satisfy the selection rules (e.g. Bretherton, 1964)

$$\mathbf{m} \pm \mathbf{m}' \pm \mathbf{m}'' = \mathbf{0}, \tag{1}$$

where $\mathbf{m} = m^n$ is the wavenumber with zonal wavenumber m and meridional wavenumber n. The relative importance of the individual triad to the dynamical evolution of the flow will depend on the degree to which the resonance condition is met, which states that the time scale of nonlinear interactions should be much shorter than the dispersion time scale, or

$$\omega \pm \omega' \pm \omega'' \ll \langle\omega\rangle. \tag{2}$$

In this condition, ω, ω' and ω'' are the drift frequencies of the wave modes constituting the triad, and $\langle\omega\rangle$ is a typical drift frequency of the modes. As Bretherton (1964) has shown, the resonance condition is also a function of the amplitude of the wave modes.

In a situation where the dominant mode is $\mathbf{m} = 3^1$, these two competing mechanisms can be captured by a highly truncated model in a rectangular zonally periodic channel with a rectangular truncation of six zonal modes and two meridional modes. Satisfying both the zonal and the meridional component of Eq. (1) implies that the complete sets of triads involving $3^1, 2^1, 4^1$ are, (a) for the long-wave route: $\{(3^1|2^1|1^2), (3^1|4^1|1^2)\}$, and (b) for the harmonic route: $\{(6^2|4^1|2^1), (6^1|4^1|2^2), (6^1|4^2|2^1)\}$. In this study, such a truncation was chosen as the starting point to investigate the respective ranges of possible behaviour exhibited by the two proposed mechanisms. Recent laboratory experiments by Früh and Read (1996) support the notion that these few interaction terms, together with zonal flow-wave interactions, can to a large extent explain the observed dynamics. It is expected that at least for the restricted range of parameters studied in the laboratory, such a model might describe the qualitative behaviour and bifurcations of the flow adequately. Once flows have been found which are qualitatively similar to observed flows, the relative importance of the triads shown in Fig. 1 and zonal flow-wave interactions can be investigated by reducing this model and thereby eliminating selected triads.

1.2 The laboratory experiment

The laboratory experiments which complement this numerical study were carried out with a thermally driven rotating annulus. The reader is referred to Früh and Read (1996) for a complete presentation of the experimental results; only a few flow types relevant to the numerical study are summarised in this section. In the apparatus shown in Fig. 2, a cylindrical fluid annulus is differentially heated in the horizontal and rotated about its vertical axis of symmetry. With the imposed temperature difference and the rotation rate of the apparatus, a stability parameter Θ and the Taylor number $\mathcal{T}$, the two principal dimensionless parameters, can be defined. The stability parameter, sometimes referred to as a Burger number or thermal Rossby number and related to the rotational Froude number, is defined by

$$\Theta \equiv \frac{g\alpha\, d\, \Delta T}{\Omega^2 (b-a)^2}, \tag{3}$$

where g is the acceleration due to gravity, α the volume expansion coefficient, ΔT the imposed horizontal temperature difference, Ω the rotation rate, and d, a, b the height, and the inner and outer radius of the annulus respectively. The Taylor number is usually defined by

$$\mathcal{T} \equiv \frac{4\Omega^2 (b-a)^5}{\nu^2 d}, \tag{4}$$

where ν is the kinematic viscosity. The dimensions of the apparatus and typical experimental parameters are listed in Table 1.

Table 1. Dimensions and typical experimental parameters of the laboratory experiment.

outer radius	a	$25mm$
inner radius	b	$80mm$
fluid depths	d	$140mm$
volume expansion coefficient	α	$4.0 \times 10^{-4}/K$
kinetic viscosity	ν	$3.2 \times 10^{-4} m^2/s$
rotation rate	Ω	$0.5 \ldots 3.0\, rad/s$
temperature difference	ΔT	$4 \ldots 30\, K$
Taylor number	$\mathcal{T}$	$10^6 \ldots 10^7$
thermal Rossby number	Θ	$0.1 \ldots 1.0$

Well known flow regimes observed in this baroclinic fluid are axisymmetric flows, steady and vacillating waves, and irregular flow ('geostrophic turbulence') as described by e.g. Hide and Mason (1975). More recently, a modulated amplitude vacillation (MAV) regime was found among the regular waves which was consistent with low-dimensional chaos (Read et al., 1992).

Upon increasing Θ or $\mathcal{T}$ from the 3MAV regime, a flow regime termed 3/2I (see Früh and Read, 1996) was found in which the modulation of wave 3 became more pronounced and less regular, and the weaker modes became stronger. In particular, mode $m = 2$ showed intermittent large-amplitude bursts, which coincided with the collapse of the vacillation of $m = 3$, followed by an approximately exponential recovery of the vacillation. This, and the bursting of $m = 2$, can be seen in the time series of the amplitude of modes $m = 2$ and 3 in Fig. 3. For part of the regime diagram, a hysteretic transition from the 3/2I to a weakly vacillating structural vacillation of mode $m = 2$ (2SV) was found after further increase in the bifurcation parameter. In other parts of the regime diagram, the transition to the 2SV regime occurred through an intermediate flow regime termed 2-3A, in which the flow switched at irregular intervals between the 3/2I and 2SV states.

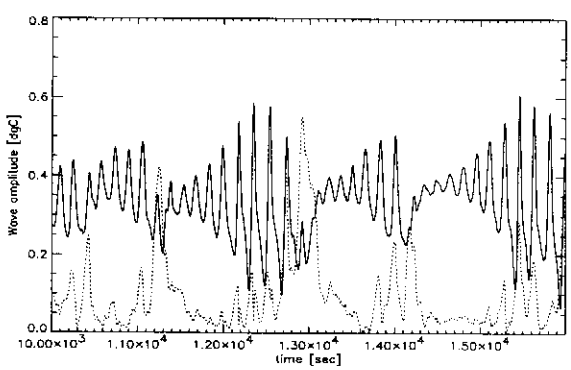

Fig. 3. Time series of wave amplitudes of modes $m = 3$ (solid line) and $m = 2$ (dashed line) from the laboratory experiments in the 3/2I regime.

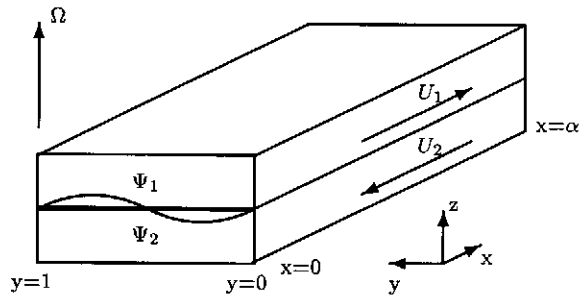

Fig. 4. The two-layer model of a quasi-geostrophic fluid in a rectangular, periodic channel.

2 Formulation of the model

2.1 Basic equations

The numerical model uses a spectral expansion of the quasi-geostrophic potential vorticity equation in two horizontal layers. The flow in typical laboratory experiments, in common with the large-scale atmospheric circulation in middle latitudes, has a sufficiently small Rossby number, $Ro \equiv U/(fL) < 0.1$, to justify the use of the quasi-geostrophic approximation. A schematic diagram of a typical two-layer model is shown in Fig. 4 where, by convention, layer 1 is at the top, and layer 2 is at the bottom. A complete derivation is given e.g. by (Pedlosky, 1987, §3.12 and Chapter 6). For a two-layer fluid, the quasi-geostrophic potential vorticity equation in each layer is

$$\left\{ \frac{\partial}{\partial t} + J(\psi_i, \, . \,) \right\} q_i = -\frac{r}{2} \nabla^2 \psi_i + \frac{1}{Re} \nabla^2 q_i \qquad (5)$$

with the potential vorticity in each layer defined by

$$\begin{aligned} q_1 &\equiv \nabla^2 \psi_1 + \beta y - F_1(\psi_1 - \psi_2) \qquad (6) \\ q_2 &\equiv \nabla^2 \psi_2 + \beta y - F_2(\psi_2 - \psi_1). \end{aligned}$$

The term $J(\psi, q)$ is the Jacobian of the two functions ψ and q defined by $J(\psi, q) = \frac{\partial \psi}{\partial x}\frac{\partial q}{\partial y} - \frac{\partial q}{\partial x}\frac{\partial \psi}{\partial y}$. The Jacobian contains nonlinear terms which account for wave interactions representing the advection of the potential vorticity by the geostrophic component of the flow field. The β-parameter is defined as $\beta = \beta^* L^2/U$. Although the laboratory experiment had flat end walls, the β-effect is included in the model since the vertical variation of the mean flow provides a contribution to the mean radial potential vorticity gradient (Hide and Mason, 1978). Since in the rotating annulus a rigid lid is in contact with the fluid, both layers have an Ekman-dissipation term of equal strength, where the parameter r is defined by

$$r \equiv \frac{\sqrt{E}}{Ro} = \sqrt{\frac{\nu f_0}{D^2}} \, \frac{L}{U} \qquad (7)$$

with the Ekman number $E = \nu/(f_0 D^2)$. The last term in Eq. (5) is the horizontal diffusion of potential vorticity, where $Re = UL/\nu = 1/(r^2 Ro)$ is the Reynolds

number. This diffusion is a parameterisation of the internal viscosity under the assumption of unit Prandtl number (Lewis, 1992). In the limit of infinite Prandtl number, the potential vorticity diffusion would be replaced by a vorticity diffusion. In the formulation of the model, the diffusion was implemented in the form of $r^2 Ro$, rather than specifying Re independently from r.
The rotational Froude number, F_i for layers $i = 1, 2$, which measures the relative importance of stratification and rotation, is defined by

$$F_i \equiv \frac{f_0^2 L^2}{g' D_i} \sim \frac{f_0^2 L^2}{N^2 D_i^2}, \tag{8}$$

where $g' = g(\rho_2 - \rho_1)/\rho_0$ is the reduced gravity, D_i the depth of layer i, and N^2 the equivalent Brunt-Väisälä frequency $N^2 = -(\partial\rho/\partial z)g/\rho$ for the continuously stratified system. The Froude number is the parameter corresponding to Θ^{-1} in the laboratory experiments. While $F = L^2/L_R^2$ with L_R as the Rossby radius of deformation, Θ can be seen as an external estimate of the Rossby radius with $\Theta = 4L_R^2/L^2$. The effective horizontal temperature difference in the fluid interior, however, is usually estimated at 10% to 20% of the imposed temperature difference.
Rather than using the equations for two coupled layers, a simple transformation converts them into coupled equations for the barotropic and baroclinic component. A barotropic and baroclinic stream function may be defined as $\psi_s \equiv (\psi_1 + \psi_2)/2$ and $\psi_d \equiv (\psi_1 - \psi_2)/2$, respectively, if the two layers have identical depth. The flow can be separated into a basic zonal flow, u_s and u_d, which are independent of y and t, and deviations from the basic flow, ψ_s' and ψ_d'. Dropping primes, the fully nonlinear equations for the barotropic and baroclinic quasi-geostrophic potential vorticity are

$$\begin{aligned} &\frac{\partial}{\partial t}\nabla^2\psi_s + \beta\frac{\partial\psi_s}{\partial x} + u_s\frac{\partial}{\partial x}\nabla^2\psi_s + u_d\frac{\partial}{\partial x}\nabla^2\psi_d \\ &\qquad + J(\psi_s, \nabla^2\psi_s) + J(\psi_d, \nabla^2\psi_d) \\ &= \; -r\nabla^2\psi_s + Re^{-1}\nabla^4\psi_s \end{aligned} \tag{9}$$

and

$$\begin{aligned} &\frac{\partial}{\partial t}(\nabla^2 - 2F)\psi_d + \beta\frac{\partial\psi_d}{\partial x} \\ &+ u_s\frac{\partial}{\partial x}\nabla^2\psi_d + u_d\frac{\partial}{\partial x}\nabla^2\psi_s + 2Fu_d\frac{\partial\psi_s}{\partial x} \\ &+ J(\psi_s, \nabla^2\psi_d) + J(\psi_d, \nabla^2\psi_s) - 2FJ(\psi_s, \psi_d) \\ &= \; -r\nabla^2\psi_d + Re^{-1}\left(\nabla^2 - 2F\right)\nabla^2\psi_d. \end{aligned}$$

2.2 Boundary conditions

Neglecting the cylindrical curvature of the annular convection chamber leads to a straight channel which is periodic in x with a 'wave length' of the mean channel length L_x. Scaling the channel such that the width $L = 1$ and the perimeter $L_x = \alpha = L_x/L$, the boundary condition of periodicity in the x-direction is

$$\psi(x, y, t) = \psi(x + \alpha, y, t). \tag{10}$$

The no-slip boundary conditions at the top and bottom of the domain are implicit in the parameterisation of the Ekman dissipation. Stewartson boundary layers which form at the vertical side walls are generally assumed to be passive in the rotating annulus; impermeable but slippery side walls are usually assumed as the boundary condition for the interior at $y = 0, 1$ (see Mundt et al., 1995, for the effect of no-slip boundary conditions at the sidewalls). The velocity normal to the side walls, v, has to vanish at the boundaries. For the quasi-geostrophic approximation the geostrophic wind, $v^{(0)}$, and the first-order ageostrophic component, $v^{(1)}$, have to be specified, with $v^{(0)}$ as

$$v^{(0)} = \frac{\partial\psi}{\partial x} = 0, \qquad \text{at } y = 0, 1. \tag{11}$$

Since $v^{(1)}$ does not appear explicitly in the equations, the last boundary condition has to be formulated as

$$\lim_{X\to\infty} \frac{1}{2X}\int_{-X}^{X} \frac{\partial^2\psi}{\partial t\partial y}\, dx = 0, \qquad \text{at } y = 0, 1. \tag{12}$$

This formulation was introduced by Phillips (1954) to ensure that there is no unspecified energy flux through the side walls.

2.3 Pseudo-spectral representation

The barotropic and baroclinic components of the stream function, ψ_s and ψ_d respectively, are expanded in a series of orthogonal functions, which all individually satisfy the boundary conditions,

$$\begin{aligned} \psi_{s,d} = &\sum_{n=1}^{N} \phi(t)_{s,d}^{n} \cos n\pi y \\ &+ \sum_{m,n=1}^{M,N} \left(\chi(t)_{s,d}^{mn} \cos\frac{2m\pi}{\alpha}x + \sigma(t)_{s,d}^{mn} \sin\frac{2m\pi}{\alpha}x\right) \\ &\sin n\pi y. \end{aligned} \tag{13}$$

The ϕ^n are the N modes describing the zonal flow correction, and the pairs χ^{mn}, σ^{mn} are the $N \times M$ wave modes with zonal wave number m and meridional wave number n.
The code, which was adapted from that of Lewis (1992), uses a 4^{th}-order Adams-Bashforth-Moulton method (e.g. Press et al., 1993), which is a predictor-corrector routine with the corrector applied once. The present code was shown to be stable for very long integrations
($> 10^4$ time steps, see Lewis, 1988). To avoid the cumbersome evaluation of the nonlinear terms in spectral space, the spectral transform technique (Orszag, 1970) was used; the stream function is projected by an inverse Fast Fourier Transform onto a spatial grid,

where the Jacobian can be computed locally, after which the results are then re-converted back into spectral representation. Interactions between the zonal flow and waves are problematic in that the coupling term has the form $\cos(n\pi y)$, whereas the waves are represented only by $\sin(n\pi y)$ terms to satisfy the lateral boundary conditions. Similarly, the zonal flow correction is of the form $\sin(n\pi y)$, while the zonal flow eigenfunctions are $\cos(n\pi y)$. Thus one has to express $\sin(n\pi y)$ in terms of $\sum_l c_{nl}\cos(l\pi y)$ and vice versa which involves the evaluation of

$$c_{nl} = 2\int_0^1 dy \sin n\pi y \cos l\pi y = \frac{2}{\pi}\left(1-(-1)^{n+l}\right)\frac{n}{n^2-l^2}.$$

The zonal flow correction by a single mode m^n will contribute to all odd meridional modes of the zonal flow. In fact, if the sum of meridional modes of the wave is even, the contribution to the zonal flow correction is in the odd modes and vice versa. The effect of the severe truncation of the models described in the following was tested without any noticeable difference in the results (cf. eg. with model Iva versus IVb described below in §2.4 and §6.2).

2.4 Hierarchy of models

The effect of different types of wave interactions and of specific wave triads could be studied either by a suitable choice of the truncation or by the suppression of appropriately selected wave modes. Model configurations which only resolved the gravest meridional mode of the waves—i.e. {(m,n)=(1,1), (2,1), (3,1), ...}—could not sustain any triad interactions because no combination of these modes would satisfy the radial component of the triad selection rules. The effect of removing a specific triad interaction was also investigated by setting the amplitude of one of the members to zero.

With these configurations, a hierarchy of models, listed in Table 2, was used to examine the role of wave coupling (a) via harmonic modes, (b) via the long wave, or (c) through wave-zonal flow interactions only. The starting point was a model with a rectangular truncation of $M = 6$, $N = 2$, which was capable of showing all of these interactions. Results for this model, hereafter referred to as the 'full' model or model I, are presented in §4.

With $m = 3$ as the dominant mode, its harmonic, $m = 6$, which provided one of the possible routes to transfer energy to the sidebands, $m = 2$ and $m = 4$ (see Fig. 1 b), could be suppressed by reducing the truncation to $M = 5$, $N = 2$. The other route, via the long wave (see Fig. 1 a), could be eliminated by setting the wave modes with $m = 1$ to zero. A last triad coupling modes $m = 3$ and $m = 2$, not previously considered in the literature, is the triad (5|3|2). These selective models, denoted as models IIa to IId, are discussed in §5.

The most restricted models (models III and IVa to IVd) eliminated all triad interactions by retaining only the gravest meridional wave modes ($n = 1$). These are in the following referred to as the 'small' models and summarised in §6. Several configurations of the models were used with a varying number of zonal wave modes as well as with different numbers of zonal flow modes.

Table 2. Modes included in the different models.

Model	I			
zonal flow	(0,1), (0,2)			
wave modes	(1,1), (1,2) (2,1), (2,2) (3,1), (3,2) (4,1), (4,2) (5,1), (5,2) (6,1), (6,2)			
Model	IIa	IIb	IIc	IId
zonal flow	(0,1), (0,2)	(0,1), (0,2)	(0,1), (0,2)	(0,1), (0,2)
wave modes	(1,1), (1,2) (2,1), (2,2) (3,1), (3,2) (4,1), (4,2) (5,1), (5,2)	(1,1), (1,2) (2,1), (2,2) (3,1), (3,2) (4,1), (4,2)	(2,1), (2,2) (3,1), (3,2) (4,1), (4,2) (5,1), (5,2) (6,1), (6,2)	(2,1), (2,2) (3,1), (3,2) (4,1), (4,2) (6,1), (6,2)
Model	III			
zonal flow	(0,1)			
wave modes	(1,1) (2,1) (3,1) (4,1)			
Model	IVa	IVb	IVc	IVd
zonal flow	(0,1)	(0,1) ... (0,6)	(0,1)	(0,1)
wave modes	(1,1) (2,1) (3,1)	(1,1) (2,1) (3,1)	(2,1) (3,1)	(1,1) (2,1)

3 Linear stability analysis

The first instability observed in this system is the instability of the imposed baroclinic shear flow with respect to small perturbations. The line of marginal stability of the zonal flow not only separates the axisymmetric regime from the wave regimes, but it also give information on the unstable wave numbers and their respective growth rates, as long as the amplitude of the waves is small. From this, one obtains some information on which wavenumber is likely to dominate the flow, although in large-amplitude solutions it is frequently observed that the equilibrated solution has a lower wavenumber than the wave with the largest growth rate (Hart, 1981). Nevertheless, it is a useful guide for choosing appropriate parameters in the integrations.

3.1 Stability condition

The linear stability analysis presented in this section is an extension of the analysis of Pedlosky (1987, §7.9 to §7.12) to incorporate the β-effect, Ekman layers and horizontal diffusion simultaneously. A derivation of the stability criterion is given in Appendix A.

The assumed basic state is a constant vertical shear flow, u_d as defined for Eqs. (9) and (10), independent of x and

Table 3. Parameters of main laboratory experiments and model configurations.

Model	u_s	u_d	α	F	β	r
I	0.5	0.5	6,10	90	0.01	0.2-0.4
IIa-IId	0.5	0.5	10	90	0.01	0.23, 0.3
III, IVa,b	0.5	10	0.05	10-100	0.01-2.0	0.01-0.4
IVc	0.5	0.5	6,10	35	2.0	0.01-1.0
IVd	0.5	0.5	6,10	19	2.0	0.01-1.0
laboratory	$10^{-2}cm$		≈ 7	$30-100$	$<10^{-2}$	$0.5-1.5$

y. Normal modes which satisfy the boundary conditions are of the form

$$\psi_{s,d} = A_{s,d}^{mn} \sin(l_n y)\, e^{ik_m(x-ct)} \tag{14}$$

with $l_n = \pi n$, $k_m = 2\pi m/\alpha$, and α the horizontal aspect ratio. Inserting the normal modes into the linearised equations gives, after some algebra, the criterion for marginal stability as

$$(K^2+F)\frac{r}{k_m} + (K^2+2F)\frac{K^2}{k_m Re} = Im\left\{\sqrt{(K^4-4F^2)\,u_d^2 + F^2\left(\frac{\beta}{K^2}+i\frac{r}{k_m}\right)^2}\right\} \tag{15}$$

with a total wavenumber K defined as $K^2 \equiv k_m^2 + l_n^2$.

3.2 Model parameters

On the basis of typical experimental conditions and the results from the linear stability analysis, suitable values for the model parameters were chosen which are listed in Table 3. Most sets of integrations were performed with r and F as the principal bifurcation parameters while Ro, β, α, u_s, and u_d were held fixed. The horizontal diffusion term, proportional to $1/Re$, was expressed as $r^2 Ro$ and thereby changed consistently with the dissipation parameter r.

Using the dimensions given in Table 1 and assuming a width of the boundary layers of $5mm$ leads to an effective aspect ratio of $\alpha = 7.3$ for the laboratory experiments. Two extreme values of α were chosen, α=6 and α=10, though the results did not appear to be sensitive to α. The imposed shear flow was scaled to have unit amplitude, which implies $u_d = 0.5$. Ro was taken to be constant at 0.05 consistent with a typical value for the annulus. A small, but non-zero, value of β, $\beta = 0.01$, was chosen to represent the residual β-effect due to the structure of the mean flow.

Following the argument in relating Θ to a measure of the Rossby radius of deformation, one would expect flows observed at $0.5 \leq \Theta \leq 0.7$ to be found in a range of $30 \lesssim F \lesssim 100$. Within these limits, F was determined from the linear stability analysis where possible, or by trial and error, to give flows with the desired dominant wavenumber.

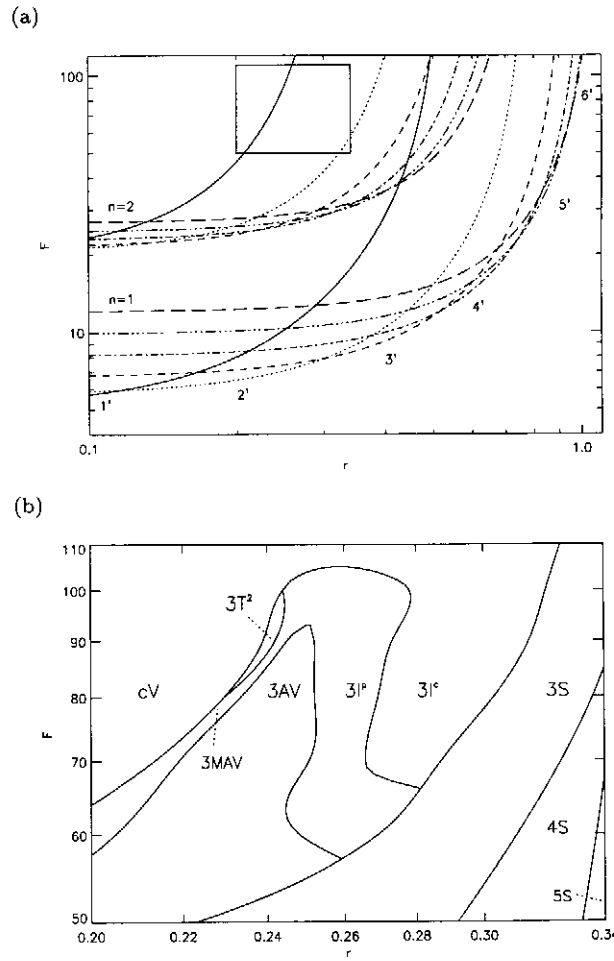

Fig. 5. Model I: a) $r-F$-plane with curves of marginal stability for the wave modes in the model and results from the regime survey. The numbers m^n label the curves of marginal stability of the wave mode with zonal wavenumber m and meridional wavenumber n. The box indicates the part of the regime diagram shown in detail in (b): (b) Detailed regime diagram; 3S, 4S, 5S: steady waves, AV: amplitude vacillation, MAV: modulated amplitude vacillation, T^2M: torus-doubled MAV, $3I^p$, $3I^c$: periodic and chaotic intermittent bursting, and cV: chaotic vacillation.

4 The full model

4.1 Regimes

After the linear stability for two meridional modes of the first six zonal wave modes was computed, the parameter space was surveyed in the range indicated in the linear stability diagram in Fig. 5(a) ($10 \leq F \leq 110$ and $0.1 \leq r \leq 2.0$). Following the first Hopf bifurcation from axisymmetric flow to a steady wave with a wavenumber corresponding to that indicated in Fig. 5(a), a sequence of mode transitions occurred to steady waves with successively lower wavenumbers until time-dependent behaviour of the wave amplitudes developed. Part of the wavenumber transitions and the time-dependent flows discussed here are shown in the regime diagram in Fig.

Table 4. Main sequence of integrations with model I at $F = 90$.

flow regime	range of r	ω_v	ω_m $\times 10^{-2} U/L$
3S	$r > r_A = 0.3144$	—	—
$3I^c$	$r_A > r > r_B = 0.273$	5.6	0.04...0.19
$3I^p$	$r_B > r > r_C = 0.255$	5.4	0.19...0.4
3AV	$r_C > r > r_D = 0.245$	5.2	—
3MAV	$r_D > r > r_E = 0.242$	5.1	0.58...0.635
$3T^2M$	$r_E > r > r_F = 0.239$	5.1	0.635
cV	$r_F > r$	5.0	0.2, 0.7

5(b). The abbreviations of flow regimes used in the following are S for a steady wave, AV for amplitude vacillation, MAV for modulated amplitude vacillation, T^2M for torus doubled MAV, I for intermittent bursting, and cV for irregular vacillation.

In the detailed discussion of the regimes, the dissipation parameter r will be the pricipal bifurcation parameter, while the Froude number is fixed at $F = 90$. The results from this set of integrations, together with the bifurcation values of r, labelled r_A to r_F, are summarised in Table 4. Unless mentioned otherwise, $F = 90$ will be assumed throughout the rest of §4 and §5.

The sequence of wavenumber transitions was terminated at r_A, where the mode $m = 3^1$ suddenly developed a strongly modulated amplitude vacillation, and all other modes became active in intermittent bursts; this flow type is referred to as '3I', and is discussed in detail in §4.2. Decreasing r further, the modulation became faster and, after an initial increase in complexity, more regular and weaker until, at r_C, the solution became a quasi-periodic mixed-mode amplitude vacillation with $m = 3^1$ as the dominant mode (termed 3AV). For $F = 90$, the 3AV regime was observed only over a very small range of r, after which the AV developed a modulation again (3MAV). In a very small range of F around $F = 90$, the 3MAV underwent a torus-doubling bifurcation ($3T^2M$) at r_E, which then bifurcated directly to a chaotic vacillation (cV) at r_F. For all other values of F, the 3MAV became directly chaotic without any intermediate bifurcations.

4.2 Intermittent bursting, 3I

Decreasing r from the steady $m = 3$ regime resulted at r_A in a sudden transition to a complex mixed-mode state, denoted $3I^c$. A time series of wave amplitudes in this regime ($r = 0.3$) is shown in Fig. 6. This flow was dominated by a vacillating mode $m = 3$, the strength of which was strongly modulated, as measured by the vacillation index, following Read et al. (1992)

$$\eta_v \equiv \frac{A_{max} - A_{min}}{A_{max} + A_{min}} \tag{16}$$

When η_v approached its maximum, all other modes in the model were also found to grow rapidly in a short burst from less than 10^{-5} up to $\approx 50\%$ of the mean

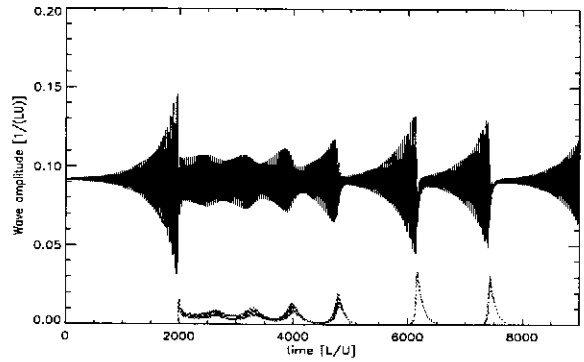

Fig. 6. Model I: Time series of the wave amplitude of modes 3^1_{bt} (solid line) and 2^1_{bt} (dotted line) at $r = 0.3$.

amplitude of $m = 3$, at which point the vacillation collapsed. Subsequently, the secondary modes decayed while the vacillation of $m = 3$ slowly gathered strength again. The vacillation period, $\tau_v \approx 20L/U$, did not vary significantly with r, while the bursting period varied from $\tau_i \approx 250L/U$ for $r = 0.26$ to over $5000L/U$ for $r = 0.31$. The time between bursts, as well as the burst amplitude, was irregular for any given value of r above $r_B = 0.273$.

The variability of both the average frequency and amplitude of the bursts, ω_i (Fig. 7 a) and η_v^{max} (Fig. 7 b) respectively, had a maximum well within the $3I^c$ regime. From the bifurcation at r_A, the variability increased until $r \approx 0.3$ and then decreased again until, at r_B, there was no variability detectable any more in either ω_i or η_v^{max}. The average modulation frequency also shows a change in the scaling at r_B with a scaling in the irregular $3I^c$ of

$$\langle \omega_i \rangle \propto (r_A - r)^{0.8 \pm 0.04}, \tag{17}$$

and a scaling in the regular $3I^p$ regime of

$$\langle \omega_i \rangle \propto (r_A - r)^{1.5 \pm 0.05}. \tag{18}$$

The value of the exponent, which is very sensitive to the choice of the critical bifurcation parameter, was determined to $r_A = 0.3144 \pm 0.0004$, and the stated error includes the uncertainty in r_A. The scaling of ω_i in Eq. (17) is in good agreement with the scaling of the bursting frequency observed in the laboratory by Früh and Read (1996), who observed for the bursting in the 3/2I regime $\omega_{i,exp} \propto \gamma^{0.7}$, where γ measured the distance from the point of bifurcation from the 3MAV to the 3/2I regime. The histogram in Fig. 7 (c) shows the relative distribution of modulation cycle times for $r = 0.307$, in the chaotic regime. Most common were comparably short periods, but there was no sharp fall-off for longer modulation periods or any indication of a well-defined upper limit.

For r smaller than r_B, the intermittently bursting flow seemed to be quasi-periodic, denoted as $3I^p$, which is

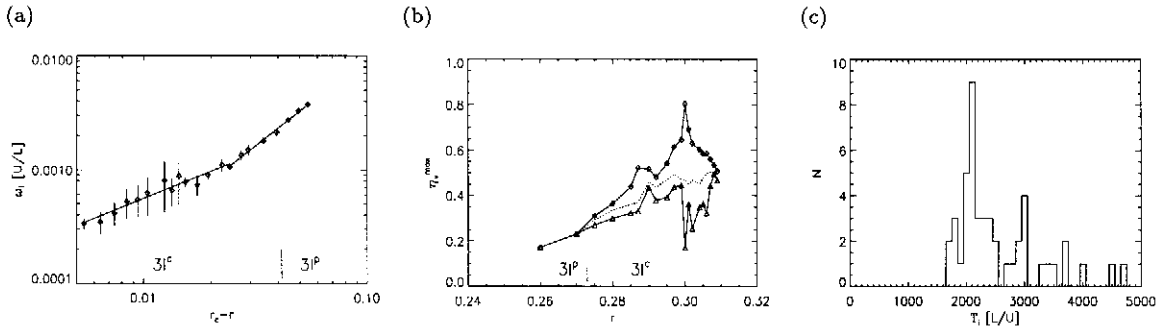

Fig. 7. Model I: (a) Scaling behaviour of the average modulation period as a function of dissipation. (b) The maximum of the vacillation index, η_v^{max}, during a modulation cycle against dissipation; plotted are its maximum, minimum, and mean. The ranges of the two regimes 3I/P/ and 3I/C/ are indicated in (a) and (b). (c) Histogram of the time between bursts for $r = 0.307$.

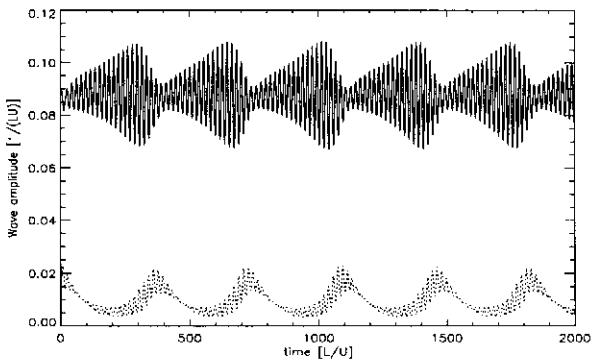

Fig. 8. Model I: Time series of the wave amplitude of modes 3^1_{bt} (solid line) and 2^1_{bt} (dotted line) at $r = 0.27$.

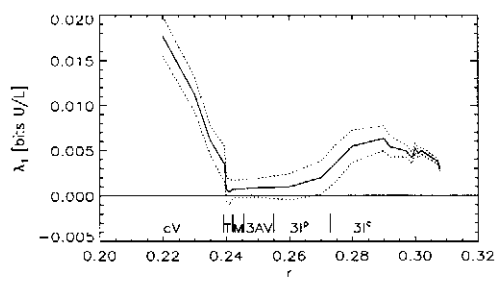

Fig. 9. Model I: Largest Lyapunov exponent against r for model. The regimes are indicated, where T is used to denote the T^2M regime, and M the 3MAV regime.

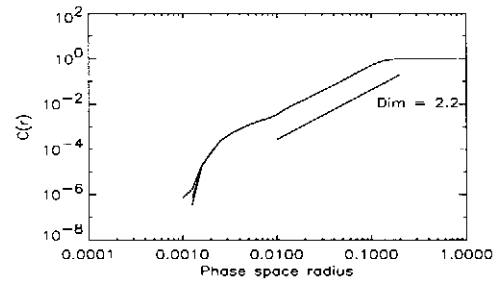

Fig. 10. Model I: Correlation integral for the 3I regime in model I, at $r = 0.27$; the almost perfectly coincident lines show the correlation integral for embedding dimensions $d_e = 3, 5, 7, 9, 11$, and the straight line, slightly displaced to the right, shows a slope consistent with a correlation dimension of $d_c = 2.2$.

illustrated in the time series of the wave amplitudes of 3^1_{bt} and 2^1_{bt} at $r = 0.27$ in Fig. 8. The largest Lyapunov exponent, shown in Fig. 9, which had a distinct positive maximum in the $3I^c$ regime, decreased rapidly from $\lambda_1 = 6 \times 10^{-3} \pm 10^{-3} bits$ per L/U at $r = 0.29$ through the $3I^p$ regime towards the periodic 3AV regime at $r = 0.25$, where it was indistinguishable from zero within the computed error. This change, however, was not reflected in the correlation dimension: dimension calculations using the Grassberger and Procaccia (1983) algorithm gave estimates of $d_c = 2.2 \pm 0.1$ for all flows in both 3I regimes (shown in Fig. 10 for $r = 0.27$).

Plotting both the maximum amplitude return map and the minimum amplitude return map on the same graph in Fig. 11 illustrates the qualitative change between $3I^c$ and $3I^p$. These return maps plot the maximum, or minimum, of the wave amplitude from one vacillation cycle against the respective extremum from the previous vacillation cycle. The diagonal line in each frame indicates the identity map, corresponding to the case where the maximum does not change from one vacillation cycle to the next, as in a pure amplitude vacillation. Points to the left of the line denote an increase in the vacillation, points to the right correspond to a decrease. While for

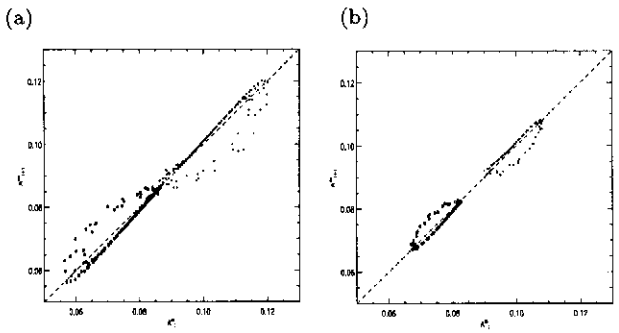

Fig. 11. Model I: Return maps of successive maxima and minima of the amplitude of wave 3: (a) $r = 0.28$, (b) $r = 0.275$, (c) $= 0.27$.

$r < r_B$, the curves of successive maxima and minima formed two well separated closed loops, they seem to have collided above r_B. If the steady wave 3 solution observed for $r > r_A$, still exists as an unstable solution, this phenomenon can be explained by a collision of the attractor with the unstable 3S solution, a mechanism known as a 'crisis' (e.g. Grebogi et al., 1982). A crisis often leads to a sudden increase in the complexity of the flow and of the attractor dimension. The existence of an unstable 3S solution at the touching point of the circles in Fig. 11 (a) and (b), with at least one weakly unstable direction, would also explain the slow growth of the vacillation near the steady solution. This fixed point would be a saddle with some attracting directions because, once the modulation collapsed, the flow converged rapidly towards the 3S.

4.3 Torus-doubling and irregular flow

Upon further decrease of r, from r_B down to r_C, the modulation gradually became weaker until, at $r = r_C$, the solution was consistent with a quasi-periodic amplitude vacillation dominated by $m = 3$ (3AV). This 3AV was not a pure $m = 3$ flow, but all other modes in the model were active and vacillated at the same frequency as $m = 3$. In a very quick succession of bifurcations the 3AV gave way to an irregular vacillation, first developing a periodic modulation (3MAV) at $r = r_D$. This 3MAV then underwent a torus-doubling bifurcation at $r = r_E$, illustrated in the maximum amplitude return maps in frames (a) and (b) of Fig. 12 respectively at $r = 0.242$ and 0.240. At $r = r_F$, the doubled torus showed the first indications of breaking up (frame c) rather than undergoing a second doubling bifurcation, and by $r = 0.235$ the torus interior was completely filled out, as shown in frame (d) of Fig. 12.

Below r_F, the flow was still dominated by the $m = 3$ mode, though the vacillation of all waves was much more irregular than in the chaotic $3I^c$ regime. This flow regime is denoted as cV, with a time series shown in Fig. 13 for $r = 0.23$. The modulation now seems to occur at a

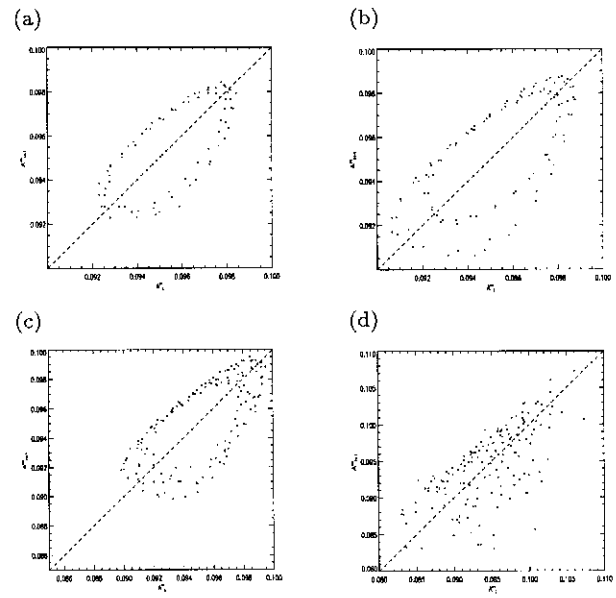

Fig. 12. Model I: Return maps of maximum amplitudes of mode $m = 3^1_{bt}$ for the transition from 3MAV to cV; (a) $r = 0.242$, (b) $r = 0.240$, (c) $r = 0.2395$, (d) $r = 0.235$.

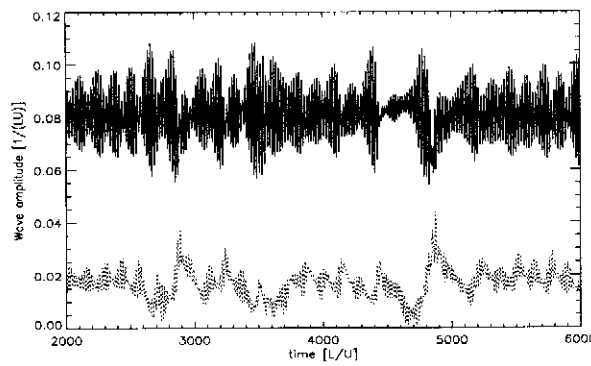

Fig. 13. Model I: Time series of the wave amplitude of modes 3^1_{bt} (solid line) and 2^1_{bt} (dotted line) at $r = 0.23$.

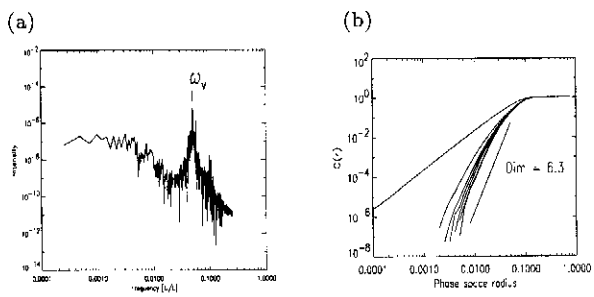

Fig. 14. Model I: (a) Power spectrum and (b) correlation integral in the cV regime at $r = 0.23$; the curved lines show the correlation integral for embedding dimensions $d_e = 3, 5 \ldots 15$ (from left to right), and the straight line, slightly displaced to the right, shows a slope consistent with a correlation dimension of $d_c = 6.3$.

relatively high frequency: $\omega_m \approx 7 \times 10^{-3} U/L$ compared to $\omega_m < 4 \times 10^{-3} U/L$ in the 3I regimes. The power spectrum of the wave amplitude time series (Fig. 14 a), however, only shows a very broad, continuous spectrum at low frequencies besides the distinct, broadened peak at the vacillation frequency, $\omega_v = 5.0 \times 10^{-2} U/L$. The higher complexity of this regime is reflected in the correlation dimension, which showed indications of scaling at around $d_c \approx 6.3 \pm 0.3$ (Fig. 14 b), and is also evident in the rapidly increasing Lyapunov exponent of $\lambda_1 = 1.8 \times 10^{-2} \pm 10^{-3} bits$ per L/U at $r = 0.22$ (Fig. 9 and $\lambda_1 \approx 5 \times 10^{-2} bits$ per L/U at $r = 0.20$, without any indication of reaching a final saturation level. Though this constitutes a fairly high dimensional flow, the required embedding dimension of $D \geq 13$ is still much smaller than the number of degrees of freedom of even this highly truncated low-order model, which consists of a set of fifty-two coupled ordinary differential equations.

4.4 Phase locking

To estimate the strength of nonlinear wave interactions of baroclinic waves in the laboratory experiments, Früh and Read (1996) introduced a *phase locking probability density function* ('locking density'), $\rho_{\mathbf{m}-\mathbf{m}'-\mathbf{m}''}$ and ρ_m for coupling through resonant triads or sideband interactions respectively. The formula used to evaluate the locking density is given in Appendix B. The triad locking density, $\rho_{\mathbf{m}-\mathbf{m}'-\mathbf{m}''}$, essentially counts the number of time steps for which the triad phase locking function $\varphi_{\mathbf{m}-\mathbf{m}'-\mathbf{m}''} \equiv \phi_{m^n} - \phi_{m^{n'}} - \phi_{m^{n''}}$, has a specific value—provided the amplitudes of the relevant modes are within a pre-selected amplitude range. For independent modes, $\rho_{\mathbf{m}-\mathbf{m}'-\mathbf{m}''}$ would be expected to have a flat distribution with $\rho_{\mathbf{m}-\mathbf{m}'-\mathbf{m}''} \approx 1/(2\pi)$ over its range of $0 \ldots 2\pi$, while a distinct peak in $\rho_{\mathbf{m}-\mathbf{m}'-\mathbf{m}''}$ indicates significant phase coherence. In the cases presented here, the coupling can be regarded as strong if $\hat{\rho}_{\mathbf{m}-\mathbf{m}'-\mathbf{m}''} \equiv \max(\rho_{\mathbf{m}-\mathbf{m}'-\mathbf{m}''}) \geq 1.0$. These arguments also extend to the sideband phase locking function Φ_m and its respective sideband locking density ρ_m. All flow regimes described above showed pronounced sideband phase locking which is apparent in the clear maximum of the density function ρ_3 of $\hat{\rho}_3 \geq 1.0$ at $\Phi_3 \equiv 2\phi_{3^1_{bt}} - \phi_{4^1_{bt}} - \phi_{2^1_{bt}} \approx \pi$. Figure 15 shows the sideband locking probability density function, ρ_3 in Fig. 15 (a), and several triad locking probability density functions in Fig. 15 (b)-(i), for $r = 0.27$ in the $3I^p$ regime. ρ_3 in frame (a) has a clear peak at $\Phi = \pi$ and falls off to zero on either side, whereas the phase locking of the harmonic triad (6|4|2) in (b) and the triad (5|3|2) in (c) have smaller peaks, with $\hat{\rho}_{6-4-2} \approx \hat{\rho}_{5-3-2} \approx 0.6$, at $\varphi = \pi$ and $3\pi/2$ respectively. These peaks are superimposed on a relatively strong background with a value of $\rho \approx 0.2$.

The maximum of $\hat{\rho}_{3-2-1} = 1.05$ at $\varphi_{3-2-1} = 3\pi/2$ for the lower sideband/long wave triad (3|2|1) in (d)

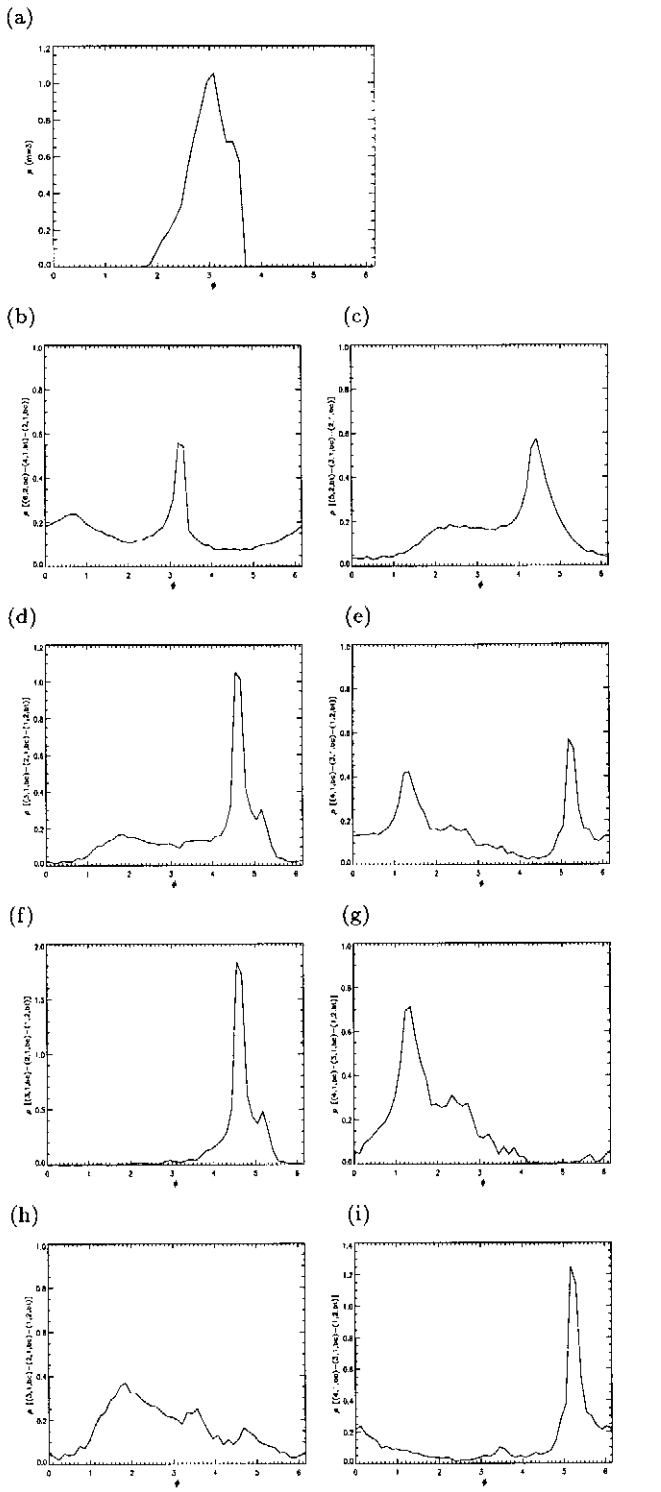

Fig. 15. Model I, $3I^p$ regime at $r = 0.27$: Locking density for (a) Φ_3, (b) (6|4|2), (c) (5|3|2), (d), (f), (h) (3|2|1), and (e), (g), (i) (4|3|1). (d) and (e) show ρ over all amplitudes of $m = 3^1_{,}$ (f) and (g) show ρ over time steps when $m = 3$ strong ($A_3 > \overline{A}_3$), and (h) and (i) when $m = 3$ weak.

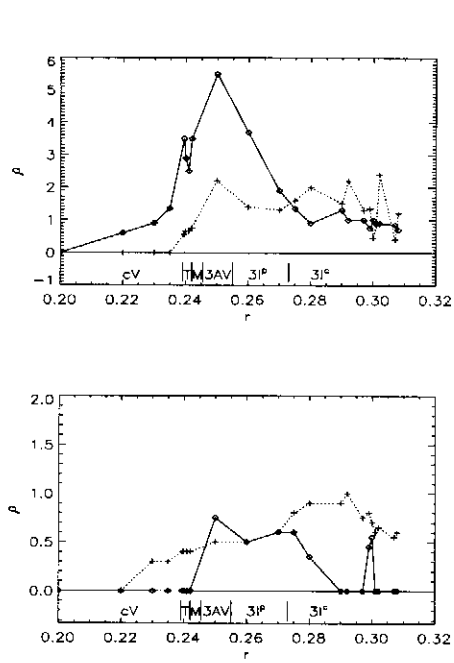

Fig. 16. Model I: Maxima of the triad locking density as a function of r for (a) (3|2|1) (solid line) and (4|3|1) (dotted line), and (b) (6|4|2) (solid line) and (5|3|2) (dotted line). Note the different scale of (a): (0...6) and (b): (0...2). The regimes are indicated, where T is used to denote the T^2M regime, and M the 3MAV regime.

is as large as that of $\hat{\rho}_3$, while the other long wave triad (4|3|1) in (e) has a bimodal structure in ρ_{4-3-1}. Frame (g) shows the contribution to ρ_{4-3-1} when the dominant component, $m = 3^1$, is strong, and (i) shows the contribution when $m = 3^1$ is weak. This separates the two phase locking regimes completely with preferred locking at $\varphi \approx \pi/2$ when $m = 3^1$ is strong, and very strong locking at $\varphi \approx 13\pi/8$ otherwise. In this analysis, the average amplitude of $m = 3^1$ was chosen as the crossover point from a strong to a weak $m = 3^1$, and this separation was also applied to ρ_{3-2-1}. The lower long wave triad showed very strong phase coupling when $m = 3^1$ was strong with $\rho_{3-2-1}(3\pi/2) = 1.9$ in (f), but only weak coupling for a weak $m = 3^1$ with a very broad maximum of $\rho_{3-2-1}(\approx \pi/2) = 0.4$ in (h). Therefore, at any time, the difference between φ_{3-2-1} and φ_{4-3-1} is consistent with $\Phi_3 = \varphi_{3-2-1} - \varphi_{4-3-1} \approx \pi$, the value observed for Φ_3, although the role of the two triads varies during a vacillation cycle. During half the cycle—when $m = 3^1$ is stronger than average—the lower sideband receives most energy, but during the other half, the upper sideband is preferred.

When the bursting was most irregular, i.e. near $r = 0.3$, the triad alternation turned into a triad competition. Figure 16 (a) shows $\hat{\rho}^{\text{strong}\,3}_{3-2-1}$ and $\hat{\rho}^{\text{weak}\,3}_{4-3-1}$ as it varies over r. At some values of r (0.3 and 0.307), the otherwise strong locking in (4|3|1) became very weak. In these cases, both long wave triads showed strong phase locking together when $m = 3^1$ was strong. At $r = 0.3$ this also resulted in dramatically improved locking in the harmonic triad, as can be seen in Fig. 16 (b). Otherwise, the harmonic triad was not active at all in the $3I^c$ regime and showed only moderate phase coherence in the $3I^p$ and 3AV regimes. It disappeared rapidly at the transition to 3MAV at r_D. The triad (5|3|2), also in Fig. 16 (b), on the other hand, had the best locking in the $3I^c$ regime, and then gradually lost coherence towards lower r. These two triads, however, are always much weaker than the two triads involving the long wave, $m = 1^2$. Especially the long wave triad with the lower sideband, (3|2|1), became very strong after the transition to $3I^p$, and even retained some phase coherence some way into the cV regime, together with (5|3|2). The other long wave triad, (4|3|1), lost all phase coherence at the transition to the cV regime.

The upper sideband/long wave triad almost always showed good phase locking in the 3I and 3AV regimes with $1 \leq \hat{\rho}_{4-3-1} \leq 2$, when $m = 3^1$ was weak (except for the cases mentioned above where the triad was active when $m = 3^1$ is strong). Towards the cV regime, however, this phase coherence reduced, and finally disappeared at r_F. While in the $3I^c$ regime the upper sideband/long wave triad was the strongest, in the $3I^p$ regime the lower sideband/long wave triad $(3^1|2^1|1^2)$ rapidly increased its phase locking until, in the 3AV flow, it reached its maximum of $\hat{\rho}_{3-2-1} = 5.5$ (see Fig. 16 a). Even in the irregular cV regime this triad retained some phase locking for some time, although by $r = 0.2$ this triad too showed no phase coherence any more.

4.5 The regime diagram; a summary

Before individual triad interactions and mean flow interactions are investigated, the results for $F = 90$ will be extended to the $r - F$-plane shown in the regime diagram in Fig. 5(b).

For small F, the transitions are straightforward in two successive Hopf bifurcations from 3S to 3AV and then to 3MAV, before the three-torus breaks up and becomes chaotic.

At $F \approx 57$, the first Hopf bifurcation becomes subcritical, together with the emergence of a reversed supercritical hopf bifurcation from the 3AV to the $3I^p$. With increasing F, this reversed Hopf bifurcation and the Hopf bifurcation for $3AV \leftrightarrow 3MAV$ move closer until they merge and disappear at $F \approx 92$. Both bifurcations, leading to MAV and $3I^p$from 3AV, are not simple Hopf bifurcations but rather *generalised* Hopf bifurcations (Golubitsky and Langford, 1981) since the emerging frequency does not remain constant but varies substantially over the entire range of the regime. The frequencies increase strictly monotonically with decreasing r. Towards the transition from 3I to 3S the modulation frequency becomes very small and seems to approach zero in a ho-

Table 5. Models II compared to model I

Model	IIa	IIb	IIc	IId
	no $m = 6$	no $m = 5, 6$	no $m = 1$	no $m = 1, 5$
$r = 0.3$	no change	no change	4I	4I
$r = 0.23$	more regular	irregular	4+cV	3+M

moclinic bifurcation.
The chaotic bursting regime, $3I^c$, is created from the $3I^p$ through an attractor crisis (e.g. Grebogi et al., 1982), in which the torus of the $3I^p$ regime collides at the centre with the unstable 3S solution. For large F, the line of the crisis bifurcation connects with the torus instability which leads to the cV flow, Although there is some difference between the chaotic flow at large r ($3I^c$) and small r (cV) at $F = 110$, it is difficult to determine a distinct transition between them.

5 Selected Triads

The analysis of the phase coherence in terms of the locking density supported the role of the long wave, $m = 1$, as the prominent mediator coupling the sidebands to the dominant wave $m = 3$ over a wide range of conditions. This conclusion can be tested further by eliminating specific wave triads from model I. This section shows results from these special models, which are summarised in Table 5. Parameters and unperturbed initial conditions were taken from the two chaotic regimes of the full model: a) $3I^c$ at $r = 0.3$, and b) cV at $r = 0.23$.

5.1 Model IIa: $m = 6$ eliminated

In model IIa the triad supported by James et al. (1981) was removed. The solution in the $3I^c$ regime did not show any qualitative difference from the full model, but the integration in the cV regime was much more regular. The flow is very similar to the solution of model I at $r = 0.2395$ (cf. Fig. 12 c), and an integration of model IIa at $r = 0.225$ resulted in a cV-type solution. All integrations exhibit the same phase locking characteristics as model I for the sidebands and the remaining triads. The 3AV flow, which showed good harmonic phase locking in model I, was also reproduced in model IIa, which suggests that the observed harmonic locking in model I is a passive element of the dynamics. Altogether, it is found that the removal of the modes with zonal wave number $m = 6$ does not affect the dynamics and with it, that the harmonic triad (6|4|2) is not essential for the observed wave coupling.

5.2 Model IIb: $m = 5$ and $m = 6$ eliminated

This configuration is an even stricter truncation of model I, in which only triads involving the long wave are permitted. As in the preceding section, the integration at $r = 0.3$ produced qualitatively the same behaviour as the full model. At $r = 0.23$, the similarity between this model and model I broke down, and the transitions below r_D were not reproduced. Though the triad (5|3|2) is considerably weaker in the full model than the lower sideband triad (3|2|1), it appears from this model that it is nevertheless an essential part of the dynamics for the transitions from the 3AV to the cV regime.

5.3 Model IIc: $m = 1$ eliminated

Model IIc was designed to exclude the sideband instability as formulated by Plumb (1977) and supported by Hide et al. (1977), while permitting the harmonic wave coupling observed by James et al. (1981). At $r = 0.3$ the model settled into an intermittent bursting with $m = 4^1$ rather than 3^1 as the dominant mode. It is possible that the omission of the long wave removed an energy sink for the baroclinic shear flow so that the zonal flow had to redistribute the available potential energy, with the result that $m = 4^1$, rather than $m = 3^1$, was the most unstable mode.
For weaker dissipation, $r = 0.23$, this model behaved very differently from any flow type found in model I. Removing the modes with a zonal wave number of $m = 5$ (model IId) did not affect the results further.
It appears that in the absence of the long-wave triads, other wave triads can to some extent take their place and lead to a modified type of intermittent bursting.

6 Zonal flow interactions

The mean flow correction by the waves was the last class of nonlinear interaction terms investigated in this study.

6.1 Model III

Model III represents the wave modes $\mathbf{m} = \{1^1, 2^1, 3^1, 4^1\}$ beside the zonal flow correction $\mathbf{m} = 0^1$. Under identical values of model parameters as for the previous models, I and II, the intermittent bursting regime was lost and replaced by a periodic amplitude vacillation. As we saw in §5.2, the removal of modes shifted the dominant wave mode to a higher wavenumber. Similarly, in model III a steady $m = 4$ wave bifurcated to a 4AV at $F = 90$ and $\beta = 0.01$. At lower values of the Froude number, $F < 65$, the 4S gave way to a 3S solution, which in turn either developed an amplitude vacillation or continued the sequence first to 2S and then to 1S. A modulated vacillation was only found for very small values of r, $r \approx 0.1$, growing from a periodic multi-mode amplitude vacillation.
As β was increased, the extent of the steady wave regimes relative to time-dependent flows was progressively reduced. Especially the modulated vacillation regime gradually expanded and shifted to smaller F and larger r, thus moving closer to the steady wave regimes. At

$\beta = 2.00$ and $20 < F < 40$, the transition from a steady $m = 3$ was directly to a bursting regime. This transition from 3S to 3I at $F = 30.0$, $r = 0.2464$ was very similar to the transition observed in model I, with a sudden onset of the large-amplitude vacillation of $m = 3$, modulated at a very low frequency, together with the bursting of the other wave modes. The scaling of the bursting frequency as a function of $r_c - r$ was found by linear regression to follow the relation of

$$\omega_i \propto (r_c - r)^{0.7\pm0.1} \tag{19}$$

with a correlation coefficient of 0.995. Before we discuss these results in the context of the full model I, a final set of models of even further restricted truncations will be presented in §6.2.

6.2 Models IV

In this set of models, the minimal models for the bursting flow are formulated by removing even more modes; in model IVa, the wave modes $\mathbf{m} = \{1^1, 2^1, 3^1\}$ were included, and this was further reduced to just two zonal modes, namely $\mathbf{m} = \{2^1, 3^1\}$ in model IVc and $\mathbf{m} = \{1^1, 2^1\}$ in model IVd. Since the wave-zonal flow interactions are the essential terms in these models, the sensitivity of the models to the representation of the zonal flow correction terms was tested in model IVb by retaining a larger number of meridional modes of the zonal flow. The results from model IVb were identical to those of model IVa in the regimes tested, and it was concluded that a single cross-channel mode of the zonal flow correction was sufficient to capture the dynamics of the investigated flows. Models with a single zonal mode were also tested, but no solutions similar to the intermittent bursting were found.

At the large value of β, $\beta = 2$, at which model III exhibited the direct transition from the steady wave regime to the intermittent bursting, all models IV also showed this direct transition. In model IVc, with $m = 2, 3$, the transition was between 2S and 2I, and in model IVd, with $m = 1, 2$, it was between 1S and 1I. The bursting frequency was found to scale as $\omega_i \propto (r_c - r)^{0.53\pm0.1}$ for model IVc, with $r_c = 0.2675$ and a correlation coefficient of over 0.99. Model IVd, with $r_c = 0.1428$, showed scaling behaviour slightly closer to those observed in the previous models with $\omega_i \propto (r_c - r)^{0.62\pm0.06}$.

7 Discussion

In Sections 4 and 5 we studied the role of resonant triad interactions in establishing complex multi-mode solutions. The primary sequence of regimes, as r was decreased, was

$$3S \leftrightarrow 3I^c \leftrightarrow 3I^p \leftrightarrow 3AV \leftrightarrow 3MAV \leftrightarrow 3T^2M \leftrightarrow cV. \tag{20}$$

A bifurcation analysis of a single-mode model by Lovegrove (in preparation) has shown that a steady wave may lose stability in a subcritical Hopf bifurcation. The divergence of the modulation period in the 3I regime towards the bifurcation to the 3S regime indicates the existence of a homoclinic orbit organising the dynamics. The nearly simultaneous existence of a Hopf bifurcation and a homoclinic orbit would suggest that we have observed a bifurcation akin to intermittency of type II (e.g. Schuster, 1995). Both the scaling of the modulation frequency as $\omega_i \propto \gamma^{0.8}$—for type-II intermittency $\omega \propto \gamma$ would be expected—, and the distribution of burst intervals (cf. Fig. 7 c) could be consistent with such a bifurcation.

Similar scaling was found in model III and in the laboratory experiments, both with $\omega_i \propto \gamma^{0.7}$, while a slightly lower scaling exponent was found in models IVc and d, $\omega_i \propto \gamma^{0.5}$ and $\omega_i \propto \gamma^{0.6}$ respectively. One should, however, be cautious in equating the flows observed in the laboratory to those found in the models; the bifurcation to the 3/2I regime in the annulus experiments was not from a 3S but rather from a 3MAV, which itself emerged either directly from the axisymmetric flow, or from a dispersive flow regime, D:

$$0 \overset{\leftarrow D \rightarrow}{\longleftrightarrow} 3MAV \longleftrightarrow 3/2I \overset{\leftarrow 2-3A \rightarrow}{\leftarrow \neq \rightarrow} 2SV. \tag{21}$$

While the 3MAV and 3/2I regimes were consistent with low-dimensional dynamics, the regimes D, 2-3A, and 2SV were not. The models discussed herein were therefore not expected to reproduce any of those flow regimes.

In the smaller models, bifurcations from a vacillating flow to the intermittent bursting were found at smaller values of β than those of the direct 3S↔3I transition. It is possible that an AV or MAV prior to the onset of the bursting—and therefore closer to the transition observed in the experiments—exists at other values of F or β, but to verify this, an extended two- or three-parameter study with the full model is required.

With the possibility of resonant triad interactions removed, it was necessary to increase β by two orders of magnitude in order to reproduce the bifurcations sequence from the 3S to 3AV in Eq. (20). Since it was shown in the models II that the further bifurcations to the cV regime depended crucially on the presence of several triads—(3|2|1), (4|3|1), and (5|3|2)—it is not surprising that none of the small models showed any of those flow regimes.

It was surprising, however, that the small models reproduced the intermittent bursting. In the full model it was found that consistent sideband phase locking was achieved through an alternation between either sideband; when the dominant mode was strong, the lower sideband was most strongly coupled, and vice versa. When the long wave was removed, as in models IIc and d, the harmonic triad could to some degree take their place and establish an intermittent bursting, though with a different dominant mode. The necessary increase in β to find the direct transition 3S↔3I suggests that β

not only affects the resonance conditions for wave-wave interaction by affecting the phase speeds of the waves, but that it also affects the efficiency of the zonal flow-wave interactions. The zonal flow correction of the baroclinic zonal flow modes due to the zonal wave mode m is of the form $(\chi_s^m \sigma_d^m - \sigma_s^m \chi_d^m)$. The χ and σ are the coefficients of the cos and sine components of ψ, respectively, as defined by Eq. (13). If β, which primarily affects the wave propagation, has a significant effect on the phase difference between the baroclinic and barotropic mode of each zonal wave, this will influence the zonal flow correction. It was observed that the phase difference in the steady wave regime increased from $\delta\phi \equiv \phi_s^3 - \phi_d^3 \approx \pi/2$ to $\delta\phi \approx 3\pi/4$ prior to the onset of the intermittent bursting.

The long-wave triads, however, seemed essential in the observed crisis bifurcation leading to the chaotic $3I^c$ in model I; the bursting solutions in all other models were quasi-periodic. While in the quasi-periodic $3I^p$ regime of the full model the lower long-wave triad was always stronger than the upper long-wave triad, in the chaotic $3I^c$ both long-wave triads were competing with comparable strengths. In the annulus experiments, it was also found that in the regular $3/2I^p$ regime the lower long-wave triad dominated the phase locking, but in the chaotic $3/2I^c$ no triad showed clear dominance.

8 Summary

In this study we have investigated complex baroclinic multi-mode flows which resulted either from wave-wave interactions through three-wave resonance, or from zonal flow-wave interactions. The flow of primary interest was a strongly modulated amplitude vacillation where the modulation was coupled with intermittent bursts of weaker wave modes. This flow appeared to involve a subcritical Hopf bifurcation and a homoclinic orbit, which would imply that this flow arose from an intermittency bifurcation of type II.

In a model representing both types of nonlinear interactions, it was found that the two triads involving the longest wave and the sidebands of the dominant wave were the triads showing the strongest wave coupling. In subsets of this model, where these two strongest triads were removed, it was shown that other triads could, for some regimes, take the place of the long-wave triads. Zonal flow-wave interactions alone were also found to reproduce a subset of the full set of multi-mode regimes, including the intermittent bursting of the weaker modes, if the value of β was significantly increased.

The findings from these modes were compared with recent laboratory experiments of multi-mode baroclinic waves in a rotating annulus experiment. While the model results do not correspond exactly to the laboratory flows, strong similarities were seen both in the wave interaction properties and in the scaling behaviour of the modulation frequency. With the model we were able to demonstrate that resonant triad interactions as well as zonal flow-wave interaction may give rise to types of fluctuations found in the laboratory. The laboratory experiments and low-order models together point to these nonlinear interactions as potential causes for some of the low-frequency variability observed in the large-scale circulation of the atmosphere in middle latitudes.

Appendix A Linear stability analysis

A1 Linearised equations

The stability of a purely zonal flow is considered. The flow has the velocities $u_1 = u_s + u_d$ in the upper layer and $u_2 = u_s - u_d$ in the lower layer. The equations describing the evolution of perturbations are the full quasi-geostrophic equations, Eqs. (9) and (10) with ψ as the perturbation. However, for small ψ the quadratic terms are negligible:

$$\left\{\left[\frac{\partial}{\partial t} + u_s\frac{\partial}{\partial x}\right]\nabla^2 + \beta\frac{\partial}{\partial x} + \left[r - Re^{-1}\nabla^2\right]\nabla^2\right\}\psi_s + u_d\frac{\partial}{\partial x}\nabla^2\psi_d = 0 \tag{A1}$$

and

$$\left\{\left[\frac{\partial}{\partial t} + u_s(\nabla^2 - 2F)\right](\nabla^2 - 2F) + \beta\frac{\partial}{\partial x} + \left[r - Re^{-1}\left(\nabla^2 - 2F\right)\right]\nabla^2\right\}\psi_d + u_d\frac{\partial}{\partial x}\left(\nabla^2 + 2F\right)\psi_s = 0. \tag{A2}$$

Perturbations $\psi_{s,d}$ of this basic state are described in terms of eigenmodes of the Laplace operator where $\psi_{s,d} \ll 1$.

$$\psi_{s,d} = A_{s,d}^{n\,m}\,\sin\left(l_m y\right)\,e^{ik_n(x-ct)} \tag{A3}$$

with $l_m = \pi m$, $k_n = \frac{2\pi}{\alpha}n$, and α the aspect ratio. Define $K^2 \equiv k_n^2 + l_m^2 = \pi^2(4n^2/\alpha^2 + m^2)$. Then, dropping the subscripts, the differential operators become

$$\frac{\partial}{\partial t} \hookrightarrow -ikc$$

$$\frac{\partial}{\partial x} \hookrightarrow ik$$

$$\nabla^2 \hookrightarrow -K^2.$$

In the following subsections I shall present a stability criterion for a uniform shear flow without any y-dependence.

A2 Uniform shear flow

The basic state does not vary across the channel, and after inserting the eigenmodes into the linearised equation, Eq. (A1) one obtains

$$\left\{ik(c-u_s)K^2 + ik\beta u_s - \left(r + Re^{-1}K^2\right)K^2\right\}A_s - ikK^2 u_d A_d = 0. \tag{A4}$$

Similarly, Eq. (A2) becomes

$$\begin{aligned} &- iku_d\left(K^2 - 2F\right)\ A_s \\ &+ \left\{ik(c-u_s)(K^2+2F) + ik\beta \right. \\ &\quad \left. - \left(r + Re^{-1}(K^2+2F)\right)K^2\right\}A_d \\ &= \ 0. \end{aligned} \tag{A5}$$

Rearranging terms yields

$$\left\{(c-u_s) + \frac{\beta}{K^2} + i\frac{r}{k} + i\frac{K^2}{k\,Re}\right\}A_s - u_d\,A_d = 0. \tag{A6}$$

and

$$\begin{aligned} &- \frac{K^2-2F}{K^2}u_d\,A_s \\ &+ \left\{\frac{K^2+2F}{K^2}(c-u_s) + \frac{\beta}{K^2} + i\frac{r}{k} + i\frac{K^2+2F}{k\,Re}\right\}A_d \\ &= \ 0. \end{aligned} \tag{A7}$$

This has non-trivial solutions if and only if the determinant of the system equals zero:

$$\begin{aligned} &\left((c-u_s) + \frac{\beta}{K^2} + i\frac{r}{k} + i\frac{K^2}{k\,Re}\right)\times \\ &\left((c-u_s) + \frac{K^2}{K^2+2F}\left(\frac{\beta}{K^2} + i\frac{r}{k}\right) + i\frac{K^2}{k\,Re}\right) \\ &\quad - \frac{K^2-2F}{K^2+2F}u_d^2 = 0. \end{aligned} \tag{A8}$$

A wave is marginally stable if the complex part of $c \equiv c_i = 0$. The perturbation grows exponentially if $c_i > 0$. Rewriting the equation as a quadratic equation for $c - u_s$ gives

$$\begin{aligned} &(c-u_s)^2 \\ &+2\left[\frac{K^2+F}{K^2+2F}\left(\frac{\beta}{K^2} + i\frac{r}{k}\right) + i\frac{K^2}{k\,Re}\right](c-u_s) \\ &= \frac{K^2-2F}{K^2+2F}u_d^2 - \frac{K^2}{K^2+2F}\left(\frac{\beta}{K^2} + i\frac{r}{k}\right)^2 \\ &-2i\frac{K^2+F}{K^2+2F}\left(\frac{\beta}{K^2} + i\frac{r}{k}\right)\frac{K^2}{k\,Re} + \left(\frac{K^2}{k\,Re}\right)^2. \end{aligned} \tag{A9}$$

After some algebra one obtains

$$\begin{aligned} c \ &= u_s \\ &- \frac{K^2+F}{K^2+2F}\frac{\beta}{K^2} \\ &- i\frac{1}{K^2+2F}\left((K^2+F)\frac{r}{k} + (K^2+2F)\frac{K^2}{k\,Re}\right) \\ &\pm \frac{1}{K^2+2F}\sqrt{(K^4-4F^2)\,u_d^2 + F^2\left(\frac{\beta}{K^2} + i\frac{r}{k}\right)^2}. \end{aligned} \tag{A10}$$

Hence the criterion for marginal stability is

$$\begin{aligned} &(K^2+F)\frac{r}{k} + (K^2+2F)\frac{K^2}{k\,Re} \\ &= \ Im\left\{\sqrt{(K^4-4F^2)\,u_d^2 + F^2\left(\frac{\beta}{K^2} + i\frac{r}{k}\right)^2}\right\}. \end{aligned} \tag{A11}$$

The growth rate of the infinitesimal wave mode is given by $k\,Im\{c\}$.

Appendix B Phase locking

From the integrated resonance condition for wave triads, Eq. (2),

$$\varphi_{\mathbf{m}-\mathbf{m}'-\mathbf{m}''} \equiv \phi_{\mathbf{m}} - \phi_{\mathbf{m}'} - \phi_{\mathbf{m}''} \approx \text{constant}, \tag{B1}$$

one can evaluate a time-averaged quantity which shows how often each value of φ (between 0 and 2π) is assumed by $\varphi_{\mathbf{m}-\mathbf{m}'-\mathbf{m}''}(t)$. This 'locking density', $\rho_{\mathbf{m}-\mathbf{m}'-\mathbf{m}''}$, may be defined as the probability density function $\rho(\varphi_{\mathbf{m}-\mathbf{m}'-\mathbf{m}''})\ d\phi$ over the data set, and gives information about the time-averaged phase locking: strong phase coherence would result in a strong peak at the preferred value of φ, while no phase coupling would give a fairly flat density function over its entire range $0 \ldots 2\pi$. If no amplitude dependence needs to be considered then the phase locking function $\varphi_{\mathbf{m}-\mathbf{m}'-\mathbf{m}''}$ at time t makes a nonzero contribution to $\rho_{\mathbf{m}-\mathbf{m}'-\mathbf{m}''}$ only at $\phi = \varphi_{\mathbf{m}-\mathbf{m}'-\mathbf{m}''}$. This can be expressed with the delta function, $\delta\left(\phi - \varphi_{\mathbf{m}-\mathbf{m}'-\mathbf{m}''}(t)\right)$, which then is integrated over time and normalised by all contributions (i.e. the limits of the time integration):

$$\begin{aligned} &\rho^*_{\mathbf{m}-\mathbf{m}'-\mathbf{m}''}(\phi) \\ &= \ \frac{1}{t_e - t_0}\int_{t_0}^{t_e} dt\,\delta\left(\phi - \varphi_{\mathbf{m}-\mathbf{m}'-\mathbf{m}''}(t)\right). \end{aligned} \tag{B2}$$

If one needs to separate the contribution from different amplitude ranges of the participating modes, then at each time the contribution to the locking density has to be weighted, either by 1 if all three modes are within their preselected amplitude window, or by 0 otherwise. This weighting is achieved by multiplying the delta function by two Heaviside functions, H, for each mode j, one setting the lower limit of the amplitude window and one the higher limit:

$$W_j \equiv H(A_j(t) - A_j^{min})H(A_j^{max} - A_j(t))lo$$

$$\text{with } H(x) = \begin{cases} 1 & \text{if } x \geq 0 \\ 0 & \text{otherwise} \end{cases}.$$

In the following equation this weighting is applied also to the normalisation factor to ensure $\int \rho d\phi = 1$. With these amplitude windows, Eq. (B2) becomes

$$\rho^*_{\mathbf{m}-\mathbf{m}'-\mathbf{m}''}\left(\phi; \{A_j^{min,\,max}\}\right) \tag{B3}$$

$$= \frac{\int_{t_0}^{t_e} dt\, \delta(\phi - \varphi(t)) \prod_j W_j(t)}{\int_{t_0}^{T} dt \prod_j W_j(t)},$$

where $j = \mathbf{m}, \mathbf{m}', \mathbf{m}''$.

In practice, $\rho_{\mathbf{m}-\mathbf{m}'-\mathbf{m}''}$ is calculated by counting the scans for which $\phi \leq \varphi_{\mathbf{m}-\mathbf{m}'-\mathbf{m}''} < \phi + \delta\phi$, provided the amplitudes of the waves are within a preselected amplitude range. The density is normalised to have unit area in the interval $0 \ldots 2\pi$:

$$\rho_{a-b-c}(\phi) = \frac{1}{\delta\phi} \times \frac{\text{no. of scans with } \left\{ \begin{array}{l} \phi \leq \varphi_{a-b-c} < \phi + \delta\phi \\ \text{and} \\ A_j^{min} \leq A_j \leq A_j^{max},\ j = a,b,c \end{array} \right\}}{\text{no. of scans with } \left\{ A_j^{min} \leq A_j \leq A_j^{max},\ j = a,b,c \right\}}. \quad \text{(B4)}$$

As in the triad phase locking, a sideband locking density, $\rho_{\mathbf{m}}$ can be defined as a measure of the time-averaged strength of the wave coupling by this mechanism with Eq. (B4), but using $\Phi_{\mathbf{m}}$ instead of $\varphi_{\mathbf{m}-\mathbf{m}'-\mathbf{m}''}$.

Acknowledgements. I wish to thank Dr S.R. Lewis for supplying me, and getting me started, with his code of the two-layer model. I am very grateful to Dr P.L. Read, Dr P. Klein and Prof R. Hide for their support and for many invaluable discussions with them. For financial support I owe thanks to the European Communities Commission for a studentship and to the UK Natural Environment Research Council for support through a research grant.

References

Bretherton, F. P., Resonant interactions between waves. The case of discrete oscillations, *J. Fluid Mech.*, *20*, 457–479, 1964.

Früh, W.-G. and Read, P. L., Wave interactions and the transition to chaos of baroclinic wves in a thermally driven rotating annulus, accepted by *Phil. Trans. Roy. Soc. Lond. A*, 1996.

Golubitsky, M. and Langford, W. F., Classification and unfoldings of degenerate Hopf bifurcations, *J. Diff. Eq.*, *4*, 375–415, 1981.

Grassberger, P. and Procaccia, I., Characterization of strange attractors, *Phys. Rev. Lett.*, *50*, 346–349, 1983.

Grebogi, C., Ott, E., and Yorke, J. A., Chaotic attractors in crisis, *Phys. Rev. Lett.*, *48*, 1507–1510, 1982.

Hart, J. E., A laboratory study of baroclinic instability, *Geophys. Fluid Dyn.*, *3*, 181–209, 1972.

Hart, J. E., Wavenumber selection in nonlinear baroclinic instability, *J. Atmos. Sci.*, *38*, 400–408, 1981.

Hide, R. and Mason, P. J., Sloping convection in a rotating fluid, *Advances in Physics*, *24*, 47–99, 1975.

Hide, R. and Mason, P. J., On the transition between axisymmetric and non-axisymmetric flow in a rotating liquid annulus subject to a horizontal temperature gradient, *Geophys. Astrophys. Fluid Dyn.*, *10*, 121–156, 1978.

Hide, R., Mason, P. J., and Plumb, R. A., Thermal convection in a rotating fluid subject to a horizontal temperature gradient: spatial and temporal characteristics of fully developed baroclinic waves, *J. Atmos. Sci.*, *34*, 930–950, 1977.

James, I. N., Jonas, P. R., and Farnell, L., A combined laboratory and numerical study of fully developed steady baroclinic waves in a cylindrical annulus, *Qr. J. Roy. Met. Soc.*, *107*, 51–78, 1981.

Klein, P., Transitions to chaos in unstable baroclinic systems: a review, *Fluid Dyn. Res.*, *5*, 235–254, 1990.

Lewis, S., R., *Long-lived eddies in the atmosphere of Jupiter*, DPhil-thesis, University of Oxford, 1988.

Lewis, S., R., A quasi-geostrophic numerical model of a rotating internally heated fluid, *Geophys. Astrophys. Fluid Dyn.*, *65*, 31–55, 1992.

Lovegrove, A. F., *Bifurcation analysis of a two-layer model*, DPhil-thesis, University of Oxford, in preparation.

Mundt, M. D., Brummell, N. H., and Hart, J. E., Linear and nonlinear baroclinic instability with rigid sidewalls, *J. Fluid Mech.*, *291*, 109–138, 1995.

Ohlsen, D. R. and Hart, J. E., Transitions to baroclinic chaos on the β-plane, *J. Fluid Mech.*, *203*, 23–50, 1989a.

Orszag, S., A., Transform method for calculation of vector-coupled sums: Application to the spectral form of the vorticity equation, *J. Atmos. Sci.*, *27*, 890–895, 1970.

Pedlosky, J., *Geophysical Fluid Dynamics*, Springer-Verlag, Berlin, Heidelberg, New York, 2nd edn., 1987.

Phillips, N. A., Energy transformations and meridional circulations associated with simple baroclinic waves in a two-level quasi-geostrophic model, *Tellus*, *6*, 273–286, 1954.

Plumb, R. A., The stability of small amplitude Rossby waves in a channel, *J. Fluid Mech.*, *80*, 705–720, 1977.

Press, W., H., Flannery, B., P., Teukolsky, S., A., and Vetterling, W., T., *Numerical Recipes*, Cambridge University Press, Cambridge, New York, 2nd edn., 1993.

Read, P. L., Bell, M. J., Johnson, D. W., and Small, R. M., Quasi-periodic and chaotic flow regimes in a thermally-driven, rotating fluid annulus, *J. Fluid Mech.*, *238*, 599–632, 1992.

Schuster, H. G., *Deterministic Chaos*, VCH Verlagsgesellschaft, Weinheim, 3rd edn., 1995.